Catalysis Science & Technology

PAPER

View Article Online
View Journal | View Issue

Cite this: *Catal. Sci. Technol.*, 2016, **6**, 2150

MeO_x/Al_2O_3 and MeO_x/CeO_2 (Me = Fe, Co, Ni) catalysts for high temperature N_2O decomposition and NH_3 oxidation†

L. G. Pinaeva,*[a] I. P. Prosvirin,[ab] L. S. Dovlitova,[a] I. G. Danilova,[a] E. M. Sadovskaya[ab] and L. A. Isupova[a]

Received 21st August 2015,
Accepted 24th October 2015

DOI: 10.1039/c5cy01381j

www.rsc.org/catalysis

A series of MeO_x/Al_2O_3 and MeO_x/CeO_2 (Me = Fe, Co, Ni) compounds was prepared by incipient wetness impregnation and characterized by XRD, XPS, UV-vis DRS, differential dissolution phase analysis (DDPA). Their activity towards N_2O decomposition and ammonia oxidation at 750–900 °C was shown to depend on oxygen mobility in the sample as characterized by steady state isotopic transient kinetic analysis (^{18}O SSITKA) and dispersion of MeO_x (Me = Fe) species. Obvious reverse "activity-FeO_x dispersion" dependence was related to the change of contribution from oxygen transfer from the support to active sites through the Me–ceria or not improbably, the Me–alumina interface. It was shown that the high efficiency of CeO_2 based samples in deN_2O can be additionally increased by CeO_2 supporting onto high surface area alumina.

1. Introduction

Secondary abatement processes of N_2O formed as an undesirable by-product during the catalytic oxidation of ammonia into nitric oxide implicates a catalyst set up in the ammonia burner operating at 800–900 °C directly after the Pt–Rh gauzes.[1] Bulk or supported mixed metal oxides were developed for catalytic N_2O decomposition and put into practice in nitric acid plants before 2000 (Co_2AlO_4/CeO_2, CuO/Al_2O_3, $La_{0.8}Ce_{0.2}CoO_3$ and Fe/ZrO_2).[1] Moreover, alternative catalytic formulations were evaluated such as yttrium-doped zirconia,[2] ceria–zirconia,[3] $A_{1-x}A'_xB_{1-y}B'_yO_3$ perovskites with A = La or Ca, B = Mn, Co or Fe, A' = Sr, B' = Cu or Ni,[4–6] metal-substituted hexa-aluminates,[7] Fe_2O_3–MeO_x (Me = Al, Zr, Ce, La, Cu, Cr) obtained by co-precipitation,[8,9] Co_3O_4 (ref. 10) and CoO_x–CeO_2 (ref. 11) obtained by calcinations of mixtures of individual oxides. The pilot plant reactor and real plant studies[8] confirmed high activity and very good mechanical stability of the Fe_2O_3/Al_2O_3 catalysts prepared by co-precipitation as well as no decomposition of nitric oxide. Several aspects with respect to the reaction mechanisms, the structure–activity correlations, the role of various gas inhibitors as well as the strategies followed to adjust the local surface structure of the abovementioned noble metal-free metal oxides were analyzed in the review of Konsolakis.[12]

Ageing of Pt–Rh gauzes is accompanied by decrease of activity and yield of NO + NO_2 (NO_x), whereas N_2O production increases. Taking account of the tendency in the last decade to reduce platinum metal loading in the reactor (including the number of gauzes and wire thicknesses), at gauzes deactivation noticeable slip of ammonia becomes possible followed by its reaction with NO_x. Therefore, development of a bi-functional catalyst that is capable of efficient N_2O abatement and NH_3 oxidation to NO_x becomes urgent for further optimization and the reduction of harmful emissions from the process of HNO_3 production.

An idea for development of an oxide-based catalyst that is capable of converting slipping ammonia with high selectivity to NO_x was successfully realized using a dual bed system, in which a Fe_2O_3–Al_2O_3-based extruded monolith followed fewer numbers of platinum gauzes.[13] Later studies showed the efficiency of these compositions in both slipping NH_3 oxidation to NO_x and N_2O abatement.[14] At the same time, Al_2O_3-based honeycomb catalysts with the same geometry and FeO_x-based active components supported by impregnation were substantially more active in both reactions and retained high activity after the run in a dual-bed system for 3 months.[14]

Earlier, we have shown that catalytic activity of Sr substituted La manganites in high-temperature N_2O decomposition correlated with the coefficient of lattice oxygen self-diffusion.[5] In the materials with high bulk oxygen mobility, the rates of oxygen transfer in the two-phase system "O_{2gas}–surface–catalyst bulk" characterized by $^{16}O/^{18}O$ exchange and N_2O decomposition additionally increased either by their decoration by structures characterized by a

[a] *Boreskov Institute of Catalysis, Novosibirsk, Russia. E-mail: pinaeva@catalysis.ru*
[b] *Novosibirsk State University, Novosibirsk, Russia*

† Electronic supplementary information (ESI) available. See DOI: 10.1039/c5cy01381j

higher rate of heteroexchange (composites $LaSrFeO_4$ (surface)–$La_{0.4}Sr_{0.6}FeO_3$ (bulk)[6]) or by modification of near surface layers by hetero-cations ($LaFeO_3$–CeO_2 composites with Fe^{3+} ions inserted into a fluorite lattice[15]). In the former case,[6] "activity – oxygen mobility" correlation was observed for reaction of NH_3 oxidation as well. Pérez-Ramírez *et al.*[16] showed that the reaction of NH_3 oxidation to NO_x over oxide catalysts (Fe_2O_3, CeO_2, Cr_2O_3) follows a Mars–van Krevelen-type scheme with participation of lattice oxygen and reoxidation of the so-formed vacancies by both gas-phase O_2 and bulk lattice oxygen. Due to this, the efficiency of NH_3 oxidation to NO_x, especially in oxygen deficient conditions, depended on the rate of bulk oxygen diffusion to surface vacancies.

In accordance with these findings, the idea to combine high activity towards N_2O decomposition and NH_3 oxidation (at high selectivity to NO_x) in the same sample was checked. In addition to $Fe/Al_2O_3(CeO_2)$ samples, Co- and Ni- supported on Al_2O_3 and CeO_2 were tried as well since a vast number of patent applications have claimed a relatively high NO selectivity (90–95%) using Co and Ni single metal oxides. Numerous attempts were made to commercialize Co_3O_4-based catalysts but substantially lower activity and reversible deactivation of Co-systems, due to reduction of Co_3O_4 by NH_3 to the inactive CoO under reaction conditions in the upper parts of the bed, excluded the replacement of Pt gauzes by oxide catalysts. Nevertheless, these systems could be tried as the second catalyst in the dual bed system, especially since the stabilizing effect of CeO_2 in Co_3O_4–CeO_2 mixed oxides with low Co content is well-known.[11] Since copper catalyzes ammonium nitrate decomposition, an extremely important safety problem may arise if copper leaches from the catalyst and accumulates in the fertilizer product.[1] This completely excludes any Cu-based system for use in the conditions of the ammonia burner, although Cu/CeO_2 revealed high efficiency in deN_2O at lower temperatures[17,18] and more probably can be located after the absorption column. In addition, it is well known that under these conditions, Cu-containing systems oxidize NH_3 to N_2 with high selectivity.

In the first stage, we showed that intrinsic catalytic activity of different Me/Al_2O_3 (Me = Fe, Co, Ni) samples obtained by impregnation towards N_2O decomposition and NH_3 oxidation was substantially lower compared to corresponding Me/CeO_2 samples with similar surface Me concentration and correlated with the rate of oxygen exchange in the samples. Variation of Fe content in the $Fe/Al_2O_3(CeO_2)$ samples revealed noticeable reverse dependence of deN_2O and NH_3 oxidation activity due to the size effect. In accordance with this, we supported FeO_x onto specially developed Al_2O_3 [19] characterized by high specific surface area, and formation of highly dispersed FeO_x at increased Fe content in the sample finally resulted in N_2O and NH_3 conversion increase. For such samples, we focused on Fe oxide as the active component because in the case of Me = Co, Ni low active $MeAl_2O_4$ or NiO_x phases were formed on the alumina surface. Using of the effect of high oxygen mobility in CeO_2 was restricted by its low surface area at the temperature of reaction, independently on preparation method.[3,11,20] Therefore, an attempt was made to disperse CeO_2 using precipitation onto high surface area Al_2O_3.

2. Experimental

2.1. Sample preparation

CeO_2 and Al_2O_3 samples used as the support were obtained by calcination of the corresponding nitrates of chemical purity (99.5%) at 900 °C for 36 h. Al_2O_3-based supports were prepared by calcination of: 1) $Al(NO_3)_3{\cdot}9H_2O$ of chemical purity (99.5%) at 1000 °C or 1200 °C for 6 h (denoted below as Al_2O_3-1000 and Al_2O_3-1200, respectively), or 2) the product of centrifugal thermal activation of commercial-grade alumina hydrate (hydrargillite)[19] at 1000 °C for 19 h (Al_2O_3-C). To obtain the Ce/Al_2O_3 support, the product of thermochemical activation of hydrargillite was first calcined at 500 °C (S_{BET} = 210 m^2 g^{-1}); then, CeO_2 was precipitated onto this product from 0.75 M $Ce(NO_3)_3{\cdot}6H_2O$ water solution using 1 M $(NH_4)_2CO_3$ as a precipitation agent, so that the Ce : Al ratio in the final product was 1 : 1 (mole). The resultant precipitate was washed until the pH of the filtrate was 7, dried at 60 °C overnight, followed by calcination at 900 °C for 5 h.

All Me/support samples (Me = Fe, Co, Ni) were prepared by incipient wetness impregnation of the corresponding support by water solution of Me nitrate with added citric acid in 10 wt% excess to the stoichiometric amount to form the corresponding citrates and ethyleneglycol, dried in air at 150 °C for 3 h and then calcined at 900 °C for 4 h. In the commonly-used abbreviation *n*Me/support, "*n*" corresponded to Me weight content in the sample in terms of the corresponding metal, although oxide compounds obviously formed. For CeO_2 and Al_2O_3-1200, the samples with Me concentration 6.7 × 10^{19} at m^{-2} have been prepared, which corresponded to Me content of around 2.5–2.7 wt% (Al_2O_3-1200) and 0.86–0.91 wt% (CeO_2). For all supports, we also varied Fe content in the samples from 0.86 to 19.8 wt%. Bulk MeO_x were obtained by calcination of the corresponding chemical purity nitrates at 900 °C for 6 h.

2.2. Sample characterization

X-ray powder diffraction (XRD) patterns were recorded using a Bruker D8 diffractometer with Cu K_α monochromatic radiation. Each sample was scanned in the range of 2θ from 10° to 70° with a step size of 0.05° in 2θ. Surface composition of the samples was investigated by X-ray photoelectron spectroscopy (XPS) using a SPECS spectrometer with Al-K_α irradiation ($h\nu$ = 1486.6 eV). The binding energy (BE) scale was preliminarily calibrated by the position of the peaks of Au $4f_{7/2}$ (84.0 eV) and Cu $2p_{3/2}$ (932.67 eV) core levels. UV-vis diffuse reflectance spectra (UV-vis DRS) were obtained using a UV-2501 PC Shimadzu spectrometer with an IRS-250A diffusion reflection attachment in the 11 000–54 000 cm^{-1} range using BaSO4 as a reference. The edge energy (or band gap, E_g) for allowed transitions was determined by finding the intercept of the

straight line for the low-energy rise of a plot of $[F(R_\infty)\,h\nu]^2$ *versus* $h\nu$,[21] where $h\nu$ is the incident photon energy and $F(R_\infty)$ is the Kubelka–Munk function.

The method of differential dissolution phase analysis (DDPA) was used to reveal the composition of the phases (including poorly crystallized, but without information about the oxygen content therein) formed in the supported samples, including possible decoration of one phase by another.[22] For this, about 10 mg of the sample was loaded in a microreactor and dissolved in the water based solvent with the composition changing from the lower towards higher acidity in the following order: 1) HCl (pH = 2), 2) (1 ÷ 3) M HCl, while the temperature increased continuously from 20 °C to 90 °C, 3) (3.6 M) HF and running the reactor with a flow rate of 3.6 ml min^{-1}. Change of the outlet mixture composition with time was analyzed by atomic emission spectroscopy (BAIRD spectrometer) using the following spectral lines (nm) of the elements: Fe–238.2, Al–308.2, Ce–413.8, Co–238.8 with 5% accuracy of measurements at sensitivity level 10^{-3} μg ml^{-1}.

Kinetics of oxygen exchange was characterized by steady state isotopic transient kinetic analysis (SSITKA). For SSITKA experiments, the sample (g = 0.025 g) was loaded into a reactor (quartz tube, i.d. = 3 mm) and heated to 800 °C in an 0.5% vol. $^{16}O_2$ + He flow and kept at this temperature for 30 minutes, whereupon the gas mixture was replaced stepwise by the same one containing $^{18}O_2$ and Ar (1 vol%) as an inert tracer. The gas flow rate for all mixtures amounted to 16.7 $cm^3\ s^{-1}$. All responses were analyzed as time variation of the ^{18}O atomic fraction in the gas phase $\alpha_g(t) = (^{16}O^{18}O + 2^{18}O_2)/(2\Sigma O^iO^j)$, where $\Sigma O^iO^j = {}^{16}O_2 + {}^{16}O^{18}O + {}^{18}O_2$.[23]

The catalytic activity for samples with particles of 250–500 μm in size was measured in a fixed-bed U-shaped reactor (3 mm i.d. quartz tube) at ambient pressure in the temperature range 750–900 °C and contact time ~10^{-3} s. For NH_3 oxidation, a mixture of 1% NH_3 in air or 1% NH_3 + 2% O_2 in N_2 was fed to the reactor charged by 0.015 or 0.043 g of the sample (see details in the text) with a flow rate 25 l h^{-1}. Outlet mixture composition was measured by IR spectroscopy. For N_2O decomposition, a gas mixture consisting of 0.15 vol% N_2O (+3% O_2 + 3% H_2O) in He flowed through the reactor with a flow rate of 60 l h^{-1}. For samples characterized by high specific surface area (Al_2O_3-C, Ce/Al_2O_3 based), we failed to reach reasonably low values of N_2O conversion at 800 °C. Therefore, the data obtained at the same sample loading (0.038 g) and flow rate (60 l h^{-1}) were considered to analyze the effect of Fe concentration. Outlet mixture composition was analyzed by an on-line gas chromatograph with Porapack T (i.d. = 3 mm, l = 3 m) and NaX (i.d. = 3 mm, l = 2 m) columns.

3. Results and discussion

3.1. Phase composition

3.1.1. XRD analysis. Al_2O_3-1200 (Fig. 1a), Al_2O_3-1000 and CeO_2 used as the supports were single phase samples (Table 1), with values of coherent scattering area d_{XRD} calculated by the Scherrer equation much less than the particle size estimated from the BET surface area (d_{BET}). For example, for Al_2O_3-1200 d_{XRD} = 360 Å, d_{BET} = 3800 Å, while for CeO_2-680 Å and 6400 Å. TEM images of the CeO_2 sample revealed a mixture of agglomerates composed of concreted crystallites of either 100 nm or 10 nm in size.[15] The same can be reasonably supposed for Al_2O_3-1200 and Al_2O_3-1000 samples as well to explain the difference between d_{BET} and d_{XRD} values. Al_2O_3-C represented a mixture of α-Al_2O_3 (Fig. 1B, Table 1) with more dispersed θ-Al_2O_3, γ-Al_2O_3 and traces of κ-Al_2O_3. In the Ce/Al_2O_3 sample, CeO_2 phase with the same lattice parameters but expected more dispersed, than in CeO_2 sample, species, θ-Al_2O_3 and traces of γ-Al_2O_3 were detected (Fig. 1C, Table 1). Dispersion of the θ-Al_2O_3 species was about the same as in Al_2O_3-C, as follows from similar widening of peaks at 2θ of ~67° (γ-Al_2O_3 + θ-Al_2O_3), but cannot be calculated more precisely because of overlapping of its more intense peak at 2θ ~32.9° with that of CeO_2.

Although Co_3O_4 and Co–Al–O spinels are characterized by the same symmetry group, increased lattice parameters of Co compounds in $2.7Co/Al_2O_3$-1200 sample (Fig. 1A) ($a = b = c$ = 8.104 (1) Å) compared with those in the $0.91Co/CeO_2$ one or in bulk Co_3O_4 ($a = b = c$ = 8.084 (0) Å) favor formation of $CoAl_2O_4$ in the former,[24] probably in the mixture with Co_3O_4. In the $2.7Ni/Al_2O_3$-1200 and $2.5Fe/Al_2O_3$-1200 samples, additional NiO with admixture of highly dispersed Ni–Al–O compounds of spinel structure and α-Fe_2O_3, respectively, were detected. The lattice parameters of NiO and Fe_2O_3 in the supported samples were exactly the same as for bulk MeO_x (not presented in Table 1 for clarity). However, slight increase of α-Al_2O_3 lattice parameters in all Me/Al_2O_3 samples points to the probability of non-substantial Me^{n+} penetration into the alumina lattice. Taking account of the slightly larger radii of Me^{3+} ions compared with that of Al^{3+} (69–74 pm and 67.5 pm, respectively), such an assumption looks quite reasonable.

FeO_x supported on Al_2O_3-C resulted in continuous decrease of the peaks corresponding to θ-, κ-, γ-Al_2O_3 with an increase of Fe content from 2.5 to 13.2 wt% (Fig. 1b). Instead of these, a second α-Al_2O_3 phase with an increased lattice parameter ($a = b$ = 4.795 Å, c = 13.057 Å) becomes evident and increases in intensity (Table 1), which more obviously points to efficient incorporation of Fe^{3+} ions into the lattices of low temperature aluminas thus promoting their transition to α-Al_2O_3 at a lower temperature.[25] This fact agrees well with decrease of S_{BET} value from 70 $m^2\ g^{-1}$ for Al_2O_3-C to 22 $m^2\ g^{-1}$ after supporting 19.8% of Fe (pattern of the last sample not presented for brevity).

In the patterns of (0.86–0.91)Me/CeO_2 samples, traces of crystalline MeO_x were observed only for the case of Me = Co, and some α-Fe_2O_3 was detected for substantially higher Fe content (sample $2.5Fe/CeO_2$). Nevertheless, unlike alumina-based samples, neither sintering of CeO_2 nor change of CeO_2 lattice parameters were noted after Me supporting (Table 1). Considering that the radius of Fe^{3+} ions (0.049–0.078 pm,

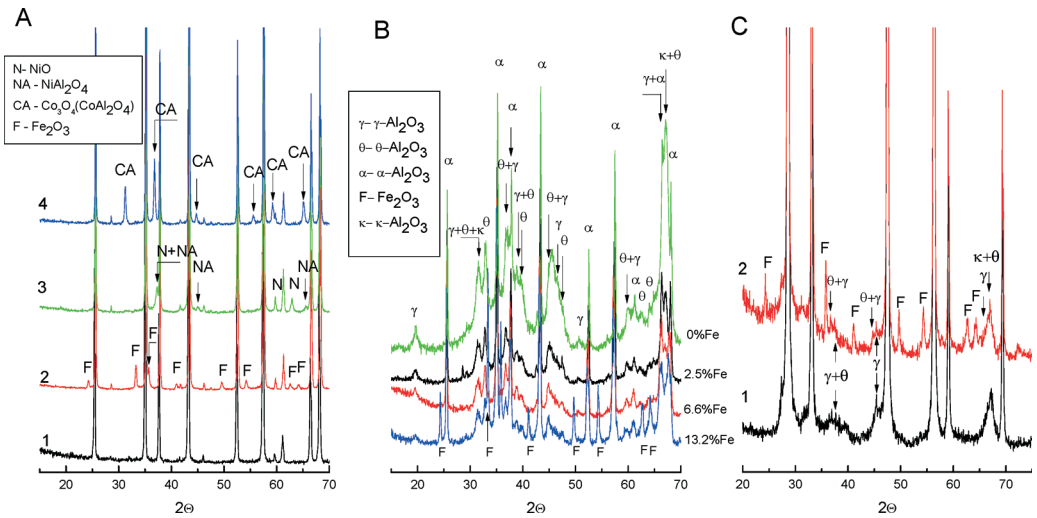

Fig. 1 XRD patterns of: (A) Al_2O_3-1200 (1) and (2.5–2.7) Me/Al_2O3-1200 (Me = Co(4), Fe (2), Ni(3)) samples, (B) Fe/Al_2O_3-C samples with different Fe content, and (C) Ce/Al_2O_3 (1) and 9.9Fe/Ce/Al_2O_3 (2) samples.

depending on coordination and spin state) is smaller than that of Ce^{4+} ions in the typical cubic fluorite lattice (0.097–0.101 nm), the expected lattice shrinkage took place at substantial Fe content in the mixed Fe_x–Ce_{1-x} oxides.[26] However, at $x < 0.05$, even slight unit cell expansion was observed and related by authors to partial Ce^{4+} reduction to the larger (1.23 Å) Ce^{3+} ion[27] during calcination in the presence of Fe^{3+}. Therefore, penetration of supporting Me into the CeO_2 lattice cannot be excluded, especially taking account of concreted nanocrystallites present in the initial support.

In the 9.9Fe/Ce/Al_2O_3 sample, α-Fe_2O_3 was detected with lattice parameters and d_{XRD} value similar to that in 13.2Fe/Al_2O_3-C and 2.5Fe/Al_2O_3-1200 samples. Although Fe supporting onto Ce/Al_2O_3 resulted in noticeable drop of the surface area, like in Al_2O_3-C based samples, it did not facilitate formation of α-Al_2O_3 (Tables 1 and 2, Fig. 1C). For similar CeO_2/Al_2O_3 samples, it was shown that it is Ce in the lower oxidation state that stabilizes alumina toward the formation of low surface area phases up to 1100 °C or 1200 °C under oxidizing and reducing conditions, respectively.[28] Since $CeAlO_3$ crystallites at high temperature and under reducing conditions were observed by XRD, stabilization of Ce^{3+} is more probably due to interaction with the OH groups of alumina. Absence of such alumina-bonded hydroxyl groups can prevent penetration of Fe^{3+} into the bulk alumina and the phase transition observed in the case of the Al_2O_3-C sample.

3.1.2. DDPA. DDPA of (2.5–2.7)Me/Al_2O_3-1200 and (0.86–0.91) Me/CeO_2 samples has been performed to reveal 1) possible modification of support lattice due to Me insertion, and 2) formation of Co–Al spinels. Al_2O_3-1200 supported samples were quite stable towards dissolution. Therefore, about 5 wt% and 2 wt% of the 2.5Fe/Al_2O_3-1200 and 2.7Co/Al_2O_3-1200 samples, respectively, dissolved during all steps (Table 2). Nevertheless, all Fe supported onto Al_2O_3-1200 passed into solution (Fig. 2A) as individual oxide/hydroxide (about 18.4 mole% of the probe dissolved in HCl), or together with some Al (~43.5 mole% of the probe dissolved in HF). Since some dissolution proceeded even after all Fe was removed from the sample, formation of Fe–Al solid solution is excluded, and the structure with FeO_x species located on the surface or on the intergrain boundaries of concreted alumina microcrystallites and linked to the last, more probably, due to penetration of some Fe^{3+} ions to the disordered near subsurface layers can be considered. In the case of 2.7Co/Al_2O_3-1200, only 0.43 wt% of Co dissolved in all steps, an overwhelming majority, as the solid solution with $Co_{0.3}Al_1$ stoichiometry reasonably relates to the mixed Co–Al–O spinel like compounds located in the near surface layer of the sample. The nature of insoluble Co compounds still remains unclear.

CeO2 did not dissolve in HCl, and very slow dissolution (about 4% of the total sample weight in 7 minutes) took place after HF feeding (Fig. 2B, Table 2). Me/CeO_2 samples dissolved in substantially milder conditions, but the character and the rate of their dissolution depended on the nature of Me. Therefore, already 95 weight% of the 0.91Co/CeO_2 sample dissolved in these conditions. Increase of solubility can be related first of all to formation of Co–Ce–O solid solution with Co/Ce = 0.004 and including all soluble Ce (dissolved in (1 ÷ 3) M HCl). This obviously means that Co^{3+} ions are able to insert into more dispersed (~10 nm) concreted microcrystallites and modify the lattice of larger (~100 nm) particles increasing their solubility. The rest of Co dissolved slowly as an oxide in the most harsh conditions (3.6 M HF) and more probably, can be related to the well-crystallized Co_3O_4 detected by XRD (Table 1). Absence of any Co in the same flow during dissolution of the 2.7Co/Al_2O_3-1200 sample points to the formation of well-crystallized Co–Al spinel therein. The quantity of 0.86Fe/CeO_2 sample dissolved was somewhat lower (54 wt% of the total) and all Fe passed into solution as it was found for 2.5Fe/Al_2O_3-1200 sample (Fig. S1†). It was included into Fe oxide/

Table 1 BET surface area, phase composition, structural parameters, and crystallite size estimated from XRD (d_{XRD}) of Al_2O_3, CeO_2 and MeO_x/$CeO_2(Al_2O_3)$ samples

Sample	S_{BET}, $m^2\ g^{-1}$	Phase composition	d_{XRD}, Å
Al_2O_3-1200	4	α-Al_2O_3 ($a = b = 4.756$ Å, $c = 12.986$ Å)	370
Al_2O_3-1000	7	α-Al_2O_3 ($a = b = 4.760$ Å, $c = 12.997$ Å)	300
Al_2O_3-C	71	α-Al_2O_3 ($a = b = 4.771$ Å, $c = 13.020$ Å)	480
		θ-Al_2O_3, κ-Al_2O_3, γ-Al_2O_3	100 (γ-Al_2O_3), 140 (θ-Al_2O_3)
2.5Fe/Al_2O_3-1200	4.0	α-Fe_2O_3 ($a = b = 5.035(0)$ Å, $c = 13.741$ Å)	260
		α-Al_2O_3 ($a = b = 4.761$ Å, $c = 12.997$ Å)	500
2.7Co/Al_2O_3-1200	4.0	$CoAl_2O_4$ or Co_3O_4 ($a = b = c = 8.104$ Å)	260
		α-Al_2O_3 ($a = b = 4.761$ Å, $c = 12.997$ Å)	520
2.7Ni/Al_2O_3-1200	4.0	NiO ($a = b = c = 4.178$ Å)	240
		$NiAl_2O_4$	≤120
		α-Al_2O_3 ($a = b = 4.760$ Å, $c = 12.996$ Å)	580
2.5Fe/Al_2O_3-C	60	α-Al_2O_3 ($a = b = 4.778$ Å, $c = 13.039$ Å)	510
		θ-Al_2O_3, κ-Al_2O_3, γ-Al_2O_3	Highly dispersed
6.6Fe–Al_2O_3-C	46	α-Al_2O_3: 31% – $a = b = 4.770$ Å, $c = 13.030$ Å	510
		69% - $a = b = 4.795$ Å, $c = 13.057$ Å	470
		θ-Al_2O_3, κ-Al_2O_3, γ-Al_2O_3	Highly dispersed
13.2Fe–Al_2O_3-C	33	α-Al_2O_3: 18% – $a = b = 4.760$ Å, $c = 13.000$ Å,	510
		82% – $a = b = 4.795$ Å, $c = 13.057$ Å,	520
		Traces of θ-Al_2O_3, κ-Al_2O_3, γ-Al_2O_3	Highly dispersed
		Fe_2O_3 ($a = b = 5.032$ Å, $c = 13.702$ Å)	250
CeO_2	1.4	CeO_2 ($a = b = c = 5.412$ Å)	680
0.91Co/CeO_2	1.4	CeO_2 ($a = b = c = 5.412$ Å)	630
		Co_3O_4 ($a = b = c = 8.084$ Å)	460
0.86Fe/CeO_2	1.4	CeO_2 ($a = b = c = 5.411$ Å)	550
0.91Ni/CeO_2	1.4	CeO_2 ($a = b = c = 5.411$ Å)	600
2.5Fe/CeO_2	1.4	CeO_2 ($a = b = c = 5.412$ Å)	650
		traces α-Fe_2O_3	—
CeO_2/Al_2O_3	63	CeO_2 ($a = b = c = 5.411$ Å)	400
		θ-Al_2O_3 and traces of γ-Al_2O_3	Highly dispersed
9.9Fe/Ce/Al_2O_3	35	CeO_2 ($a = b = c = 5.411$ Å)	460
		θ-Al_2O_3 and traces of γ-Al_2O_3	Highly dispersed
		α-Fe_2O_3 ($a = b = 5.035$ Å, $c = 13.741$ Å)	320

Table 2 Chemical composition of dissoluble part of Me/Al_2O_3-1200(CeO_2) samples (Me = Co, Fe, Ni)

Sample	Sample dissolved, weight%	Me, weight% of the sample in dissolved portion	Element	Distribution of elements dissolved during different steps but O, mole%			
				Total	HCl (pH = 2)	0.33 M HCl	3.6 M HF
2.5Fe/Al_2O_3-1200	5	2.53	Al	38.1	—	—	38.1
			Fe	61.9	—	18.4	43.5
2.7Co/Al_2O_3-1200	2	0.43	Al	82.1	—	—	82.1
			Co	17.9	0.4	—	17.5
CeO_2	4	—	Ce	100	—	—	100
0.91Co/CeO_2	95	0.93	Ce	98.2	—	98.2	—
			Co	1.8	Traces	0.39	1.41
0.86Fe/CeO_2	54	1.0	Ce	96.8		96.8	—
			Fe	3.2	0.60	1.86	0.74
0.91Ni/CeO_2	11	0.81	Ce	91.3	—	—	91.3
			Ni	8.7	Traces	7.8	0.9

hydroxide whose solubility in HCl (pH = 2) and at the substantially higher acidity (3.6 M HF) can be due to different degree of crystallinity or defect structures formed. The parallel dissolution of the remaining Fe and Ce in the flow of (1 ÷ 3) M HCl with the stoichiometry Fe/Ce = 0.02 points to formation of Fe–Ce–O solid solution, more probably, with participation of CeO_2 composites characterized by smaller sizes of crystallites. Unmodified ceria is stable even in 3.6 M HF and can be related to composites with largest crystallites. We cannot exclude that both unmodified CeO_2 and Ce–Fe–O solid solution are decorated by highly defective Fe oxide/hydroxide species dissolved in weak HCl. In the case of the 0.91Ni/CeO_2 sample (Fig. S1†), most of the supported Ni dissolved individually in (1 ÷ 3) M HCl, while the parallel Ni and Ce dissolution took place in the more rigid conditions (3÷6 M HF) and included only 10 weight% of the sample.

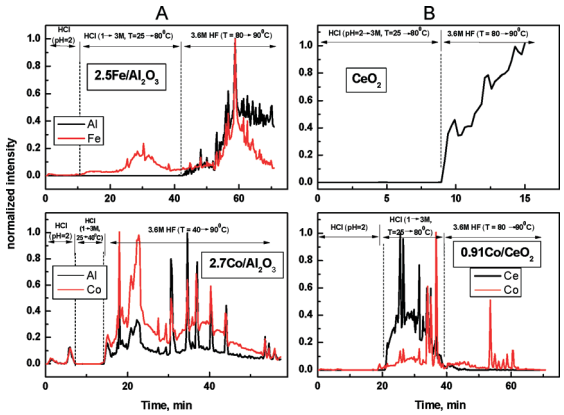

Fig. 2 DDPA spectra of: (A) 2.5Fe(2.7Co)/Al_2O_3-1200, (B) CeO_2 and 0.91Co/CeO_2 samples.

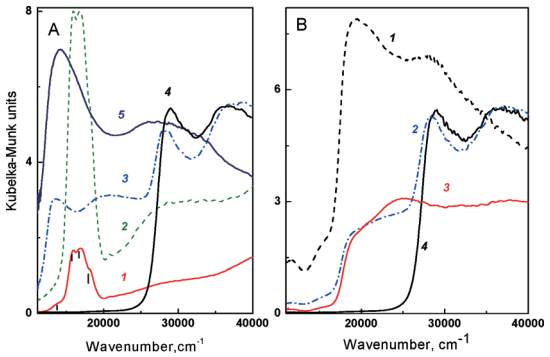

Fig. 3 UV-vis DR spectra of: A – (1) 2.9Co/Al_2O_3-1200, (2) $CoAl_2O_4$ supplied by Aldrich, (3) 0.93Co/CeO_2, (4) CeO_2, (5) Co_3O_4; and B – (1) FeO_x, (2) 0.86Fe/CeO_2, (3) 2.7Fe/Al_2O_3-1200, (4) CeO_2.

Therefore, in the 2.7Co/Al_2O_3-1200 sample, Al^{3+} ions partially replace Co^{3+} in the spinel structure, forming both highly disordered and well-crystallized Co–Al–O species, while incorporation of Fe^{3+} ions into the boundaries of the micro-composites results in the anchoring of Fe_2O_3 crystallites to the alumina surface. Me–ceria interaction results in formation of Me–Ce–O solid solutions in Me/CeO_2 samples; their content and degree of disorder in the sample change in the following order: 0.91Co/CeO_2 > 0.86Fe/CeO_2 > 0.91Ni/CeO_2 ≥ CeO_2.

3.2. Microstructure

UV-vis DR spectra of different Co- and Fe-based catalysts have been presented in Fig. 3a and b, respectively. CeO_2 was characterized by strong absorbance bands at 36 500 and 29 000 cm^{-1} attributed to $Ce^{4+} \leftarrow O^{2-}$ charge transfer and the interband transitions, respectively,[29] and a band gap energy (E_g) value of 3.35 eV, which is consistent with the reported value of 3.3 eV.[29–31] The spectra of 0.91Co/CeO_2 (Fig. 3a) and 0.86Fe/CeO_2 (Fig. 3b) samples are in fact a superposition of those for corresponding bulk oxides and CeO_2, excluding the red shift of absorption edge of CeO_2 (E_g values of 3.18 and 3.22 eV for 0.91Co/CeO_2 and 0.86Fe/CeO_2, respectively) and additional absorption band at ~20 000 cm^{-1} (Co case) and 23 500 cm^{-1} (Fe case). A minimal red shift of the absorption edge compared to that in the support was found for the 0.91Ni/CeO_2 sample (E_g value of 3.27 eV, spectrum not shown for brevity). We already observed these spectral characteristics for a Fe/CeO_2 sample prepared in the same way[15] and explained their appearance by O_2 adsorption on the structural defect, more obviously, clusters of oxygen vacancies arose after the entry of the dopant ions into the bulk of CeO_2. As proposed in,[30] a change in the value of the absorption edge indicates that either (1) Me ions in Me/CeO_2 samples substitute into the CeO_2 lattice; or (2) the isolated Me ions form a mixed Me–Ce oxide and strongly interact with CeO_2 leading to the electronic structure changes. In our case, the value of the red shift correlated well with content of Me–Ce mixed solution in the sample, as determined by DDPA.

In the spectrum of the 2.9Co/Al_2O_3-1200 sample, an intense triplet of bands at about 15 900, 17 000 and 18 200 cm^{-1} with the shoulder at 13 800 cm^{-1} was detected and related to the transitions of $^4A_2 \rightarrow {}^4T_1(^4P)$ of the tetrahedral Co^{2+} ions in Co–Al–O spinel and cobalt oxide, respectively.[32] The presence of the same triplet in the reference $CoAl_2O_4$ sample (Aldrich) supports formation of Co–Al–O spinel with admixture of Co_3O_4.

3.3. Surface composition

As follows from the X-ray photoelectron spectra of Ni 2p, Fe 2p, and Co 2p levels in Me/Al_2O_3-1200 and Me/CeO_2 samples presented in Fig. 4, the nature of Me surface compounds depends on the nature of the support. Usually, no difference between various Co compounds can be reliably drawn from binding energies of either Co $2p_{1/2}$ or Co $2p_{3/2}$ signals[10] without accounting for the position of their satellites arising due to the shake-up process of the Co^{2+} compound in the high spin state. Indeed, BE values characterizing the Co $2p_{3/2}$ peak position in CoO, CoOOH and Co_3O_4 are indistinguishable (~780.0 eV). Higher, but also very close, BE values have been reported for $CoAl_2O_4$ and $Co(OH)_2$ (781.9 and 781.2 eV, respectively).[33–38] However, for CoO, $Co(OH)_2$ or $CoAl_2O_4$, the satellite – main signal distances fall in the range 5–6.5 eV,[34,35,39,40] while the satellites in the spectrum of pure Co_3O_4 and CoOOH should be located approximately 9–10 eV away from the main signals.[34,36,39] In this regard, the BE value of the Co $2p_{3/2}$ signal at 781.6 eV with satellite at 786.6 eV in the 2.7Co/Al_2O_3-1200 sample (Fig. 4a) excluded CoO, Co_3O_4 and CoOOH from our consideration, and either $Co(OH)_2$[33] or $CoAl_2O_4$[34,37,38] could form on the surface. According to DDPA data, $Co(OH)_2$ could be responsible for about 0.4% of Co compounds (Table 2, corresponds to Co dissolved in HCl at pH = 2); therefore, most of the surface Co included in the Co–Al spinel structures. To ensure the correctness of such assignment, the spectrum of $CoAl_2O_4$ supplied by Aldrich and additionally calcined at 900 °C for 5 h

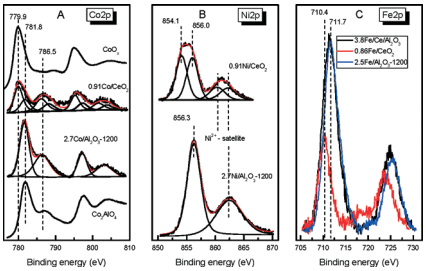

Fig. 4 (A) Co2p, (B) Ni2p, (C) Fe2p spectra of Me/Al_2O_3-1200(CeO_2) samples (Me = Co, Ni, Fe) with similar (~7 × 1019 at/m^2) concentration of Me, and Fe 2p spectrum of 3.8Fe/Ce/Al_2O_3 sample (C).

has been presented as well. In the 0.91Co/CeO_2 sample, the position of the main Co $2p_{3/2}$ peak shifted to lower BE values (779.9 eV), while the shoulder at 781.9 eV was still present resulting in the ratio of their intensities of ~3 : 2. Definite assignment of the peak at 779.9 eV to individual CoO, Co_3O_4 or CoOOH was impossible since the presence of satellites at 786.7 and 790.8 eV agrees with formation of any of these compounds. In addition, in the XPS spectrum of the bulk Co_3O_4 sample characterized by the same lattice parameters as the 0.91Co/CeO_2 sample (Table 1), the intensity of the satellite peak was substantially lower. Hence, different oxide/hydroxide-like Co compounds, including those in Co–Ce–O solid solution, have been formed on the surface of the 0.91Co/CeO_2 sample. In particular, $Co(OH)_2$ in this case could result from hydration of highly dispersed species.

The Ni $2p_{3/2}$ peak at 856.3 eV in the 2.7Ni/Al_2O_3-1200 sample (Fig. 4b) can be due to both $NiAl_2O_4$ (BE ranging from 855.2 to 857.2 eV) and $Ni(OH)_2$ (855.6–856.6 eV),[41–45] the former being detected as well by XRD (Fig. 1, Table 1). NiO state, characterized by lower BE value (854.2 eV),[45] was detected in the 0.91Ni/CeO_2 sample together with $Ni(OH)_2$ ($NiO : Ni(OH)_2$) = 1 : 1) resulting in the widening of both the main Ni 2p peak and the energy shake-up satellite peak about 6 eV above the main one. As in the 0.91Co/CeO_2 sample, $Ni(OH)_2$ detection could indicate the presence of highly dispersed NiO species both in Al_2O_3 and CeO_2-based samples. In this case, their relative content in the samples is higher compared with the Co case.

While the BE value of the Fe $2p_{3/2}$ spectra in the 0.86Fe/CeO_2 sample at 710.4 eV (Fig. 4c) indicates a preferential Fe^{3+} state in the oxide, its high energy shift (BE = 711.8 eV) detected in both the 2.5Fe/Al_2O_3-1200 specimen and all Al_2O_3-1000, Al_2O_3-1200 and Al_2O_3-C supported samples can be related to formation of Fe^{3+} oxyhydroxide.[46] In the 3.8Fe/Ce/Al_2O_3 sample, both states of Fe^{3+} have been detected also, but the fraction of Fe^{3+} state in the oxide is somewhat higher than in Fe/Al_2O_3-based samples. Therefore, FeO_x species anchor both to the Al_2O_3 and CeO_2 surfaces.

In the Ce 3d spectra of the 3.8Fe/Ce/Al_2O_3 sample, the normal complex form due to shake-down satellites from an O 1s to Ce 4f electron transfer observed for CeO_2 and 0.86Fe/CeO_2 was supplemented by the features marked as v' and u' due to anion defects and Ce^{3+} (Fig. S2†).[47] This means that besides smaller crystallized CeO_2 species, X-ray amorphous $CeAlO_3$ and probably isolated Ce^{3+} species can reasonably form after CeO_2 precipitation onto high surface area alumina,[48,49] thus stabilizing alumina toward the formation of low surface area phases, as proposed in reference.[27]

Therefore, spinel-like surface structures including Al have been formed on the surface of the 2.7Co/Al_2O_3-1200 sample and probably their mixture with $Ni(OH)_2$ in the 2.7Ni/Al_2O_3-1200 sample. It is quite reasonable to suppose that above 700 °C, surface Fe oxyhydroxide formed after Fe supporting onto Al_2O_3 and all Ni- and Co-containing hydroxylated species convert to corresponding oxides, and thus similar types of surface compounds participate in the reaction in both Al_2O_3-1200, CeO_2 and CeO_2/Al_2O_3 based samples.

Table 3 lists the data on the surface concentration of Me in the different Al_2O_3-1200 and CeO_2 based samples. Similar values were measured in the (2.5–2.7)Me/Al_2O_3-1200 and 0.91Co(0.86Fe)/CeO_2 samples with the same as related per surface unit (6.7 × 10^{19} at m^{-2}) content of Me therein that means similar MeO_x (Co–Al–O) species dispersion (D_{Me}) therein. Its relative value can be estimated as follows: $D_{Me} = Me_s/C_{Me}$, where Me_s is the surface atomic concentration of Me in the sample as measured by XPS (Table 3) [%] and C_{Me} is total content of Me in the samples [atoms/m^2]. Noticeably higher content of Ni in the near surface layers of the CeO_2 based sample can be explained either by lower degree of Ni penetration into CeO_2, resulting in the formation of Ni–Ce–O solid solutions (Table 2) or by higher dispersion of NiO_x species, which agrees well with high content of hydroxylated species.

3.4. ^{18}O SSITKA

Fig. 5 shows the time dependencies of exchanged oxygen for different samples as related to unit of the surface (N_O) calculated using the formulae

$$N_O = N_A \frac{2C_{O_2}U}{S_{BET}g}\int_0^t \left(\alpha_g^{input} - \alpha_g\right)dt$$

where α_g^{input}-isotope fraction in the inlet mixture (0.95), C_{O_2} – O_2 concentration (mol mol^{-1}), U–flow rate of the reaction mixture (mole/s), and N_A–Avogadro number. It is seen that for (2.5–2.7)Fe(Co)/Al_2O_3-1200 samples, $N_O(t)$ dependencies (at higher rate of exchange on 2.5Fe/Al_2O_3-1200, as determined from the slope of N_o curves) reached the plateau after about 15 s after isotope admission corresponding to exchanged 4.9 × 10^{20} and 3.2 × 10^{20} O atoms per g for 2.5Fe/Al_2O_3-1200 and 2.7Co/Al_2O_3-1200 samples, respectively. Taking account of the quantity of supported Me (2.7 × 10^{20} atoms per g), one can suppose that within the accuracy of measurement, solely the oxygen of Fe_2O_3 and Co oxidic compounds (Co_3O_4 + $Co_{3-x}Al_xO_4$) participated in the exchange. The integral quantity of exchanged oxygen in the 2.5Fe/Al_2O_3-C sample (7.9 × 10^{20} atoms per g) substantially exceeds that in supported Fe oxide. Provided substantially more dispersed FeO_x species have been formed in this sample compared with those in

Table 3 Physicochemical properties of different Me/Al_2O_3, Me/CeO_2 and $3.8Fe/Ce/Al_2O_3$ samples

Sample	S_{BET}, $m^2\ g^{-1}$	Me_s, at% (by XPS)	Fe_{exp}, rel. units	D_{Me}, rel. units
CeO_2 based				
$0.86Fe/CeO_2$	1.3	1.0	1.3	1.5
$0.91Co/CeO_2$	1.3	1.2	—	1.8
$0.91Ni/CeO_2$	1.3	2.0	—	2.7
$2.5Fe/CeO_2$	1.3	1.5	2.1	0.72
Al_2O_3-1200 and Al_2O_3-1000 based				
$2.5Fe/Al_2O_3$-1200	4	1.1	4.4	1.6
$2.7Co/Al_2O_3$-1200	4	1.0	—	1.5
$2.7Ni/Al_2O_3$-1200	4	1.4	—	2.1
$0.86Fe/Al_2O_3$-1200	4	1.1	4.4	4.8
$2.5Fe/Al_2O_3$-1000	7	1.4	9.8	3.7
Al_2O_3-C based				
$2.5Fe/Al_2O_3$-C	61	0.46	28.1	10.5
$6.6Fe/Al_2O_3$-C	46	1.3	59.8	8.5
$13.2Fe/Al_2O_3$-C	33	2.2	72.6	5.1
$19.8Fe/Al_2O_3$-C	22	1.6	35.2	1.7
CeO_2/Al_2O_3 based				
$3.8Fe/CeO_2/Al_2O_3$	50	1.3	65.0	16.0

$2.5Fe/Al_2O_3$-1200 one (Table 3), it is more probably support oxygen that can transfer to O_2 molecule through developed Fe-alumina interface.

Substantially more profound and faster oxygen exchange took place on CeO_2 based samples, obviously involving the bulk of the support starting from the very low time after $^{18}O_2$ admission. The rate of exchange changed in the following order: $0.91Co/CeO_2 \geq 0.86Fe/CeO_2 > 0.91Ni/CeO_2 \approx CeO_2$ and correlated with values of the red shift of the CeO_2 band gap energy (E_g) in turn depending on the content of Me–Ce mixed solution in the sample characterized by increased degree of disorder. Therefore, oxygen transfer from fluorite lattice to the surface by extended vacancies arising after insertion of Me^{n+} ions into the fluorite lattice can be responsible for enforced rate of isotope exchange on Me/CeO_2 (Me = Co, Fe) samples compared with pure CeO_2.

3.5. Catalytic activity

3.5.1. N_2O decomposition

Effect of the support nature. Among Al_2O_3-1200-based samples with similar surface concentration as supported Me

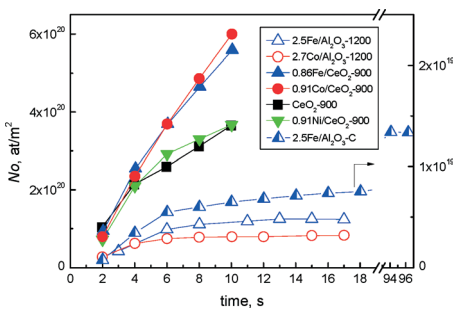

Fig. 5 Time dependence of the quantity of exchanged oxygen (N_O) in ^{18}O SSITKA experiments for different Me/Al_2O_3 and Me/CeO_2 samples.

(6.7×10^{19} at m^{-2}), catalytic activity in N_2O decomposition at T = 750–900 °C can be ordered as follows: $2.5Fe/Al_2O_3$-1200 > $2.7Co/Al_2O_3$-1200 > $2.7Ni/Al_2O_3$-1200 > Al_2O_3-1200 (Fig. 6). The (0.86–0.91)Me/CeO_2 samples with quite close, both calculated (6.7×10^{19} at m^{-2}) and real (Table 3), surface concentration of Me as in (2.5–2.7)Me/Al_2O_3-1200 samples revealed substantially higher intrinsic activity. In the case of Co and Ni containing samples such increase of the activity could be partly related to the formation of principally different state of active component (oxides/hydroxides in CeO_2 instead of corresponding Co(Ni)–Al–O spinels located on the surface of Al_2O_3). Nevertheless, a similar effect observed for Fe based samples characterized by similar type of active species on both supports obviously points to the importance of increased oxygen mobility of CeO_2, which in turn was substantially more active than Al_2O_3. The general scheme of N_2O decomposition obeys the *Langmuir–Hinshelwood mechanism*:

$$N_2O + S \rightarrow N_2O\text{-}S \quad (1)$$

$$N_2O\text{-}S \rightarrow N_2 + O - S \quad (2)$$

$$2O\text{-}S \leftrightarrow O_2 + 2S \quad (3)$$

where S is surface active site, N_2O-S is adsorbed or chemisorbed N_2O, and O-S is adsorbed or chemisorbed O, the rate of O_2 desorption by step 3) in the case of (0.86–0.91) Me/CeO_2 samples increases due to alternative fast supply of oxygen to reduced site S from the subsurface layers (O_{ss}) of CeO_2 characterized by increased bulk oxygen mobility through Me–CeO_2 interface containing many oxygen vacancies to obtain additional O-S site:

$$O\text{-}S \leftrightarrow O_{ss} + S \quad (4)$$

A similar scheme considering two alternative pathways of regeneration of active sites was also proposed for Cu/CeO_2 samples tested in substantially lower temperature range

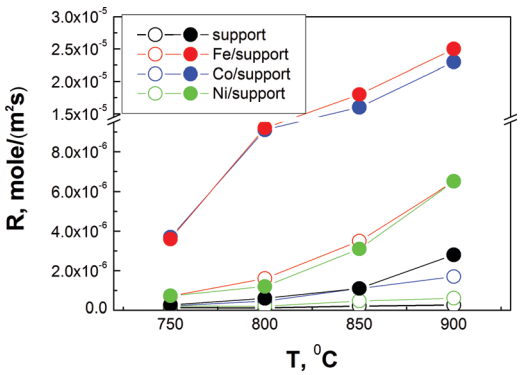

Fig. 6 Temperature dependence of the activity of different (2.5–2.7) Me/Al_2O_3-1200 (open symbols) and (0.86–0.91) Me/CeO_2 (solid symbols) samples (Me = Co, Fe, Ni) in the reaction of N_2O decomposition.

(between 300 and 550 °C) and included recombination step (if two oxidized copper sites are close enough to each other) and the step of Cu^{2+}–O-species reduction by Ce^{3+}.[50]

Effect of Fe content and FeO_x dispersion. With variation of Fe content in Al_2O_3-1200-based samples from 0.89 to 6.6 wt% (Fe was chosen as the most active among Me) we observed the inverse "activity (as related both to sample surface unit and to one Fe atom) – Fe content" dependence (Fig. 7A). The same Fe_s values for 0.86Fe/Al_2O_3-1200 and 2.5Fe/Al_2O_3-1200 samples (Table 3) indicate decrease of FeO_x species dispersion (D_{Fe}, Table 3) at higher Fe content. Finally, similar rates of N_2O decomposition were measured for bulk Fe_2O_3 and all Fe/Al_2O_3-1200 samples (Fig. S3†), although in the former case the Fe_s value should be obviously higher. Therefore, activity of surface Fe sites decreases substantially with enlargement of FeO_x species.

With variation of Fe content in CeO_2-based samples from 0.5 to 2.5 wt% (*i.e.* at similar interval of supported Fe to that in the case of Al_2O_3-1200-based samples as related per surface unit and thus similar dispersion of FeO_x species) their higher activity due to increased mobility of oxygen is more prominent at lower quantity of supported Fe. However, activity drop was substantially more prominent, although even higher Fe_s values were measured for the 2.5Fe/CeO_2 sample than for the 0.86Fe/CeO_2 one (Table 3). Supposing the rate of oxygen transfer from the bulk to active sites should depend on the length of MeO_x–CeO_2 interface, its decrease at enlargement of FeO_x species (Table 3), revealed as start of oxygen exchange at higher temperature (Fig. S4†) should make an additional negative contribution to the activity.

Effect of the support surface area. In accordance with observed effect of FeO_x dispersion on activity, use of the support characterized by higher specific surface area allows obtaining more dispersed FeO_x species at substantially higher total Fe content (Table 3). This opens up additional possibilities for increase of conversion as measured at the same sample loading. Indeed, at a similar quantity of supported Fe, N_2O conversion increased with S_{BET} value of Al_2O_3 (Fig. 7B).

Unfortunately, for Fe/Al_2O_3-C samples we failed to perform catalytic tests at reasonably low conversion values for correct calculation of the reaction rate values. This fact and substantial negative effect of the quantity of supported Fe on S_{BET} value (Tables 2 and 3) complicated analysis of parameters determining the activity. To overcome this problem, we calculated the concentration of exposable FeO_x species (Fe_{exp}) per weight unit by the following formula: $Fe_{exp} = Fe_s * S_{BET}$, where Fe_s is the surface concentration of Fe as measured by XPS (Table 3), and compared conversion values were measured for the same catalyst loading as dependent on both Fe content in the sample and Fe_{exp}. It turned out that N_2O conversion decreased with increase of Fe content from 2.5% to 19.8% (Fig. 7B) or FeO_x dispersion drop (Table 3), but this order cardinally differed from that for Fe_{exp} (13.2Fe/Al_2O_3-C > 6.6Fe/Al_2O_3-C > 19.8Fe/Al_2O_3-C > 2.5Fe/Al_2O_3-C). Therefore, similar to Fe/Al_2O_3-1200 samples, it is the size effect of FeO_x species that seems to be the dominant factor determining descending character of "conversion-Fe content" dependence. Similar reverse dependence was already observed earlier for lower (500–650 °C) temperatures.[51] Taking account of SSITKA data obtained for 2.5Fe/Al_2O_3-1200 and 2.5Fe/Al_2O_3-C samples, higher activity of smaller FeO_x species can be due to growing ability of oxygen supply to reduced active sites S from the alumina regions adjacent to developed MeO_x-alumina interface (step 4). Oxygen (3 vol%) and H_2O (3 vol%) addition into the reaction mixture, in accordance with considered abovementioned scheme of the mechanism, decreased the observed N_2O conversion, but did not change the order of activity (Fig. S5†).

Effect of CeO_2 dispersion. Using the effect of high oxygen mobility of CeO_2 for the increase of the efficiency of N_2O decomposition (Fig. 7B) is restricted by its low surface area under the reaction conditions.[3,20] Therefore, in addition to traditionally used increase of concentration of active sites by supporting more active component, we tried to disperse CeO_2 by supporting onto high surface area Al_2O_3. Only Fe oxide was used in this case to avoid formation of low active Ni (Co)–Al spinels. The 3.8Fe/Ce/Al_2O_3 and 9.9Fe/Ce/Al_2O_3 samples revealed that the highest N_2O conversion (Fig. 7B) was due to the part of FeO_x that was anchored to the surface of higher dispersed ceria particles (Table 1, Fig. 4c). At the same time, the size effect, at least for the sample 3.8Fe/Ce/Al_2O_3, cannot be completely excluded (compare D_{Fe} values in the Table 3 for the samples 3.8Fe/Ce/Al_2O_3 and 6.6Fe/Al_2O_3-C with similar S_{BET}).

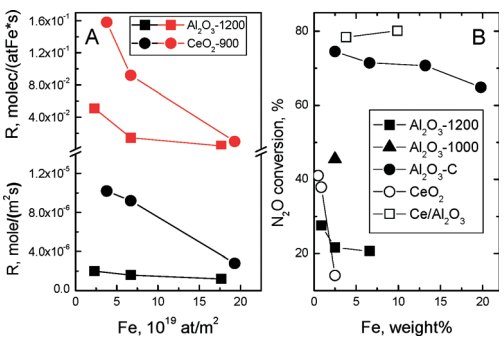

Fig. 7 Reaction rate (A) and N_2O conversion as measured at the same sample loading and flow rate (B) at 800 °C depending on Fe content in Al_2O_3-1200, Al_2O_3-1000, Al_2O_3-C, CeO_2 and Ce/Al_2O_3 based samples.

3.5.2. NH_3 oxidation

Effect of the support nature. Among (2.5–2.7) Me/Al_2O_3-1200 samples, the 2.5Fe/Al_2O_3-1200 one was the most active (Fig. 8A) and characterized by the highest selectivity to NO + NO_2 (86–88%). As a result, the orders for the activity and the efficiency of NO_x formation evaluated as NO_x *yield* = *Conversion* × NO_x *selectivity* were similar to that for the activity of N_2O decomposition: 2.5Fe/Al_2O_3-1200 ≫ 2.7Co/Al_2O_3-1200 > 2.7Ni/Al_2O_3-1200–Al_2O_3-1200. In addition, the N_2O yield value calculated in a similar manner as for NO_x *yield* on the 2.5Fe/Al_2O_3-1200 sample in this temperature interval was lower than 2%, which is comparable to that for

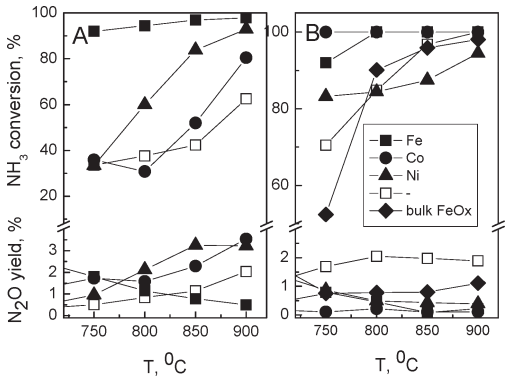

Fig. 8 Temperature dependence of NH_3 conversion and N_2O yield for (2.5–2.7) Me/Al_2O_3-1200 (A) and (0.86–0.91) Me/CeO_2-900 (B) samples. Catalyst loading 0.015 g.

Pt–Rh gauzes,[1] while continuous increase of N_2O yield with temperature was noted for all other samples. At lower O_2 concentration in the inlet mixture (2.5%), the yield of NO_x decreased to 77–78%, mainly because of lower selectivity. For Co- and Ni-based samples and for pure Al_2O_3-1200, negative changes of conversion and NO_x selectivity were substantially more prominent.

We failed to calculate the rate of ammonia oxidation in all temperature intervals due to non-differential reactor operating conditions. Hence, to compare intrinsic activity of samples characterized by different S_{BET} values, we tested catalytic properties of (0.86–0.91) Me/CeO_2 samples at catalyst loading of 0.043 g corresponding to the same surface area as for Al_2O_3-1200-based samples. In these conditions, at 750 °C, complete NH_3 conversion was measured on all (0.86–0.91) Me/CeO_2 samples, and 96% for CeO_2 that is obviously due to capability of CeO_2 itself to donate lattice oxygen for ammonia oxidation.[16] Even at the same catalyst loading as for Al_2O_3-1200-based samples (0.015 g), *i.e.* at about a 3 times lower number of Me sites therein (Table 3), higher values of NH_3 conversion were observed for corresponding CeO_2 based samples (Fig. 8B). This increase, at least in the case of Fe-based samples, is exclusively due to the ability of the support to donate oxygen to FeO_x, since substantially lower conversion values were measured on CeO_2 and bulk FeO_x characterized by similar S_{BET} values. N_2O yield values were reasonably lower than on corresponding Al_2O_3-1200-based samples. In addition, at 800 °C, the order of NH_3 conversion and NO_x yield (not shown for brevity), $0.91Co/CeO_2 \geq 0.86Fe/CeO_2 > 0.91Ni/CeO_2 \approx CeO_2$, was exactly the same as for the efficiency towards oxygen exchange therein (Fig. 4).

Strong decrease of both NH_3 oxidation[52] and N_2O decomposition[32] over Co oxide at high temperatures was shown to be due to Co_3O_4 reduction to CoO. We did not observe such deactivation of the $0.91Co/CeO_2$ sample with temperature both at N_2O decomposition (Fig. 6), as in Co_3O_4–CeO_2 mixed oxides with low Co content,[11] and at ammonia oxidation (Fig. S7B†), although Co_3O_4 reduction under TPD conditions was observed (Fig. S6†). It obviously can be explained by higher resistance of the Co–Ce interface towards reduction due to some oxygen supply from CeO_2 by reaction (4). Nevertheless, at lower temperature, the $0.91Co/CeO_2$ sample with Co state closer to Co_3O_4 was already substantially more active than $0.87Fe/CeO_2$ both in N_2O decomposition (Fig. S7A†) and NH_3 oxidation (Fig. S7B†).

Effect of Fe content and FeO_x dispersion. Decreasing dependence of NH_3 conversion *vs.* Fe content in Al_2O_3-1200 and CeO_2-based samples (0.015 g sample loading for all these experiments) was observed (Fig. 9), similarly to the reaction of N_2O decomposition, and thus can be related to size effect. Moreover, for the Fe/CeO_2 case, it was more prominent due to attenuation of oxygen transfer processes through the Fe–CeO_x interface (Fig. S4†). Nevertheless, unlike the reaction of N_2O decomposition, FeO_x dispersion is not a predominant factor for NH_3 conversion any more. Therefore, at Fe content lower than 3×10^{19} atoms per m^2 (the case with Fe/Al_2O_3-C and $Fe/Ce/Al_2O_3$ samples), the NH_3 conversion value depended mainly on the quantity of exposable Fe (Fe_{exp}).

At the same time, these were larger FeO_x species that converted NH_3 to NO_x more selectively in all Al_2O_3-based samples (Fig. S8†), finally resulting in quite similar (77–81%, in the case of Fe/Al_2O_3-1200 samples) or growing with Fe content (up to 79% for Fe/Al_2O_3-C) NO_x yield values (Fig. 9). In accordance with findings of Pérez-Ramírez and Kondratenko[16] on bulk Fe_2O_3, the desired reaction follows a Mars–van Krevelen-type scheme involving the participation of lattice oxygen in the NH_3 conversion to NO. The degree of reduction of the oxide surface was shown to determine the product distribution. One can reasonably suppose that for small species, the FeO_x surface should be in a more reduced state because of a smaller rate of dissociative activation of O_2 molecules on the Fe–Al interface. In addition, a growing contribution from low selective NH_3 oxidation on Al_2O_3 should be accounted as well.

We also believe that the more oxidized state of FeO_x anchored to CeO_2, resulting from more efficient O transfer through the Fe–Ce interface, causes higher selectivity to NO_x in the $3.8Fe/Ce/Al_2O_3$ and $9.9Fe/Ce/Al_2O_3$ samples compared to the Fe/Al_2O_3-C ones with similar dispersion. In addition, substantially smaller values of N_2O yield were measured on

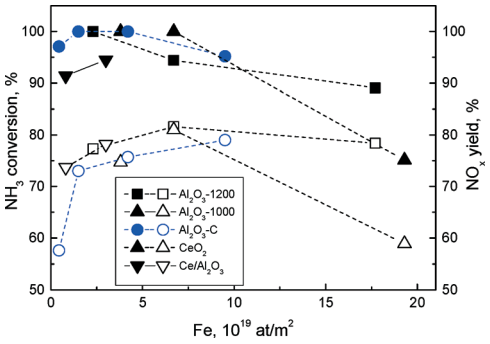

Fig. 9 Dependence of NH_3 conversion (solid symbols) and NO_x yield (open symbols) on Fe content in different $Fe/(Al_2O_3,CeO_2)$ samples. Catalyst loading 0.015 g.

$Fe/Ce/Al_2O_3$ samples, which agree with their higher activity towards N_2O decomposition.

Conclusions

We have shown that replacement of Al_2O_3 by CeO_2 as the support for MeO_x (Me = Fe, Co, Ni) characterized by increased lattice oxygen mobility resulted in substantial increase of the rates of $^{16}O/^{18}O$ exchange at 800 °C, N_2O decomposition and NH_3 oxidation on corresponding samples. Oxygen transfer from the fluorite lattice to the surface by extended oxygen vacancies arose after insertion of Me^{n+} ions into the fluorite lattice was shown to be responsible for the enforced rate of isotope exchange.

Formation of low active spinel-like Me–Al–O structures restricted the application of Co and Ni oxides in any Al_2O_3 containing catalysts. For CeO_2- and Al_2O_3-based samples with supported FeO_x, an obvious size effect was observed in both reactions. Therefore, highly dispersed FeO_x was substantially more active due to change of contribution of oxygen supply from the support (both ceria and, probably, alumina) to reduced surface sites through $Fe–CeO_x$ interface thus increasing the rate of O_2 desorption. However, smaller species oxidized NH_3 to NO_x less selectively.

Using high surface area Al_2O_3-C, the samples with high content of dispersed FeO_x in the weight unit were synthesized to increase observable N_2O conversion. To increase the surface area of CeO_2 and thus efficiently use the promoting effect of oxygen mobility, CeO_2 was dispersed onto alumina by precipitation. $Fe/Ce/Al_2O_3$ samples with optimal content of Fe revealed superior activity in N_2O decomposition and NH_3 oxidation to NO_x compared with Fe/Al_2O_3 with similar S_{BET} and dispersion of FeO_x species values.

Acknowledgements

The authors thank Mrs. I. Kharina for preparation of the Al_2O_3-C sample.

Notes and references

1 J. Pérez-Ramírez, F. Kapteijn, K. Schöffel and J. A. Moulijn, *Appl. Catal., B*, 2003, **44**, 117.
2 P. Granger, P. Esteves, S. Kieger, L. Navascues and G. Leclercq, *Appl. Catal., B*, 2006, **62**, 236.
3 P. Esteves, Y. Wu, C. Dujardin, M. K. Dongare and P. Granger, *Catal. Today*, 2011, **176**, 453.
4 D. V. Ivanov, E. M. Sadovskaya, L. G. Pinaeva and L. A. Isupova, *J. Catal.*, 2009, **267**, 5.
5 Y. Wu, X. Ni, A. Beaurain, C. Dujardin and P. Granger, *Appl. Catal., B*, 2012, **125**, 149.
6 D. V. Ivanov, L. G. Pinaeva, L. A. Isupova, E. M. Sadovskaya, I. P. Prosvirin, E. Yu Gerasimov and I. S. Yakovleva, *Appl. Catal., A*, 2013, **457**, 42.
7 J. Pérez-Ramírez and M. Santiago, *Chem. Commun.*, 2007, 619.
8 G. Giecko, T. Borowiecki, W. Gac and J. Kruk, *Catal. Today*, 2008, **137**, 403.
9 J. Kruk, K. Stołecki, K. Michalska, M. Konkol and P. Kowalik, *Catal. Today*, 2012, **191**, 125.
10 E. Wilczkowska, K. Krawczyk, J. Petryk, J. W. Sobczak and Z. Kaszkur, *Appl. Catal., A*, 2010, **389**, 165.
11 E. Iwanek, K. Krawczyk, J. Petryk, J. W. Sobczak and Z. Kaszkur, *Appl. Catal., B*, 2011, **106**, 416.
12 M. Konsolakis, *ACS Catal.*, 2015, **5**, 6397.
13 V. A. Sadykov, L. A. Isupova, I. A. Zolotarskii, L. N. Bobrova, A. S. Noskov, V. N. Parmon, E. A. Brushtein, T. V. Telyatnikova, V. I. Chernyshev and V. V. Lunin, *Appl. Catal., A*, 2000, **204**, 59.
14 L. Pinaeva, E. Sutormina, L. Isupova, N. Kulikovskaya and A. Marchuk, *RU Pat.*, 2 430 782 C1, 2010.
15 L. Pinaeva, L. Isupova, I. Prosvirin, E. Sadovskaya, I. Danilova, D. Ivanov and E. Gerasimov, *Catal. Lett.*, 2013, **143**, 1294.
16 J. Pérez-Ramírez and E. Kondratenko, *J. Catal.*, 2007, **250**, 240.
17 M. Zabilskiy, B. Eravec, P. Djinović and A. Pintar, *Chem. Eng. J.*, 2014, **254**, 153.
18 M. Konsolakis, S. A. C. Carabineiro, E. Papista, G. E. Marnellos, P. B. Tavares, J. Agostinho Moreira, Y. Romaguera-Barcelay and J. L. Figueiredo, *Catal. Sci. Technol.*, 2015, **5**, 3714.
19 L. Isupova, Yu. Tanashev, I. Kharina, E. Moroz, G. Litvak, N. Boldyreva, E. Paukshtis, E. Burgina, A. Budneva, A. Shmakov, N. Rudina, V. Kruglyakov and V. Parmon, *Chem. Eng. J.*, 2005, **107**, 163.
20 I. Danilova, E. Slavinskaya, V. Zaikovskii, A. Ivanova, A. Boronin, R. Gulyaev and Yu. Amosov, *Kinet. Catal.*, 2010, **51**, 143.
21 J. Tauc, R. Grigorovici and A. Vancu, *Phys. Status Solidi B*, 1966, **15**, 627.
22 V. Malakhov, N. Boldyreva, A. Vlasov and L. Dovlitova, *J. Anal. Chem.*, 2011, **66**, 458.
23 L. G. Pinaeva, E. M. Sadovskaya, A. P. Suknev, V. B. Goncharov and B. S. Bal'zhinimaev, in *Mass Spectrometry Handbook*, ed. M. S. Lee, Wiley, Hoboken, 2012, pp. 1229–1256.
24 S. Kurajica, J. Popović, E. Tkalčec, B. Gržeta and V. Mandić, *Mater. Chem. Phys.*, 2012, **135**, 587.
25 O. Kirichenko, V. Ushakov, E. Moroz and M. Vorob'eva, *Kinet. Catal.*, 1993, **34**, 739.
26 Z. Zhang, D. Han, S. Wei and Y. Zhang, *J. Catal.*, 2010, **276**, 16.
27 A. Gupta, A. Kumar, U. V. Waghmare and M. S. Hegde, *Chem. Mater.*, 2009, **21**, 4880.
28 A. Piras, S. Colussi, A. Trovarelli, V. Sergo, J. Llorca, R. Psaro and L. Sordelli, *J. Phys. Chem. B*, 2005, **109**, 11110.
29 A. Bensalem, J. C. Muller and F. Bozon-Verduraz, *J. Chem. Soc., Faraday Trans.*, 1992, **88**, 153.
30 R. Zhang, J. T. Miller and C. D. Baertsch, *J. Catal.*, 2012, **294**, 69.
31 R. C. Olegário, E. C. F. Souza, J. F. M. Borges, J. B. M. Cunha, A. V. C. Andrade, S. R. M. Antunes and A. C. Antunes, *Dyes Pigm.*, 2013, **97**, 113.

32 C. He, M. Paulus, W. Chu, J. Find, J. A. Nickl and K. Kohler, *Catal. Today*, 2008, **131**, 305.
33 I. G. Casella and M. R. Guascito, *J. Electroanal. Chem.*, 1999, **476**, 54.
34 H. Xiong, Y. Zhang, K. Liew and J. Li, *J. Mol. Catal. A: Chem.*, 2005, **231**, 145.
35 M. H. Kim and K.-H. Choo, *Catal. Commun.*, 2007, **8**, 462.
36 J. Yang, H. Liu, W. N. Martens and R. L. Frost, *J. Phys. Chem.*, 2010, **C114**, 111.
37 X. Duan, M. Pan, F. Yu and D. Yuan, *J. Alloys Compd.*, 2011, **509**, 1079.
38 N. Srisawad, W. Chaitree, O. Mekasuwandumrong, P. Praserthdam and J. Panpranot, *J. Nanomater.*, 2012, **2012**, 1.
39 D. Barreca and C. Massignam, *Chem. Mater.*, 2001, **13**, 588.
40 S. C. Petitto, E. M. Marsh, G. A. Carson and M. A. Langell, *J. Mol. Catal. A: Chem.*, 2008, **281**, 49.
41 D. Nikolova, R. Edreva-Kardjieva, G. Gouliev, T. Grozeva and P. Tzvetkov, *Appl. Catal., A*, 2006, **297**, 135.
42 P. Dufresne, E. Grimblot and J. P. Bonnelle, *J. Phys. Chem.*, 1981, **85**, 2344.
43 E. Laurent and B. Delmon, *J. Catal.*, 1994, **146**, 281.
44 C. Jiménez-González, Z. Boukha, B. de Rivas, J. J. Delgado, M. A. Cauqui, J. R. González-Velasco, J. I. Gutiérrez-Ortiz and R. López-Fonseca, *Appl. Catal., A*, 2013, **466**, 9.
45 P. Prieto, V. Nistor, K. Nouneh, M. Oyama, M. Abd-Leftil and R. Diaz, *Appl. Surf. Sci.*, 2012, **258**, 8807.
46 S. Suzuki, K. Yanagihara and K. Hirokawa, *Surf. Interface Anal.*, 2000, **30**, 372.
47 L. Chen, P. Fleming, V. Morris, J. D. Holmes and M. A. Morris, *J. Phys. Chem. C*, 2010, **114**, 12909.
48 J. Z. Shyu, W. H. Weber and H. S. Gandhi, *J. Phys. Chem.*, 1988, **92**, 4964.
49 C. Ge, L. Liu, Z. Liu, X. Yao, Y. Cao, C. Tang, F. Gao and L. Dong, *Catal. Commun.*, 2014, **51**, 95.
50 M. Zabilskiy, P. Djinović, E. Tchernychova, O. Tkachenko, L. Kustov and A. Pintar, *ACS Catal.*, 2015, **5**, 5357.
51 P. Pomonis, D. Vattis, A. Lycourghiotis and C. Kordulis, *J. Chem. Soc., Faraday Trans. 1*, 1985, **81**, 2043.
52 M. C. Goromonzi, S. K. Raman, B. D. Padalia, A. Manohar and P. N. Koul, *React. Kinet. Catal. Lett.*, 1980, **15**, 131.